Journal of
Mechanics of
Materials and Structures

**CALCULATION OF INERTIAL PROPERTIES OF THE
MALLEUS-INCUS COMPLEX FROM MICRO-CT IMAGING**

Jae Hoon Sim, Sunil Puria and Charles R. Steele

CALCULATION OF INERTIAL PROPERTIES OF THE MALLEUS-INCUS COMPLEX FROM MICRO-CT IMAGING

JAE HOON SIM, SUNIL PURIA AND CHARLES R. STEELE

The middle ear bones are the smallest bones in the human body and are among the most complicated functionally. These bones are located within the temporal bone making them difficult to access and study. We use the micro-CT imaging modality to obtain quantitative inertial properties of the MIC (malleus-incus complex), which is a subcomponent of the middle ear. The principal moment of inertia of the malleus along the superior-inferior axis (17.3 ± 2.3 mg/mm^3) is lower by about a factor of six in comparison to the anterior-posterior and lateral-medial axes. For the incus, the principal moment of inertia along the superior-inferior axis (35.3 ± 6.9 mg/mm^3) is lower by about a factor of two than for the other two axes. With the two bones combined (MIC), the minimum principal moment of inertia (132.5 ± 18.5 mg/mm^3) is still along the superior-inferior axis but is higher than for the individual bones. The superior-inferior axis inertia is lower by a factor of 1.3 than along the anterior-posterior axis and is lower by a factor 2 along the lateral-medial axis. Values for inertia of the MIC show significant individual differences in three human ears measured, suggesting that middle ear models should be based on individual anatomy. Imaging by micro-CT scanner is a nondestructive modality that provides three-dimensional volume information about middle ear bones at each stage of manipulation with resolution down to $10\,\mu$m. In this work extraneous tissue is removed to obtain a sufficiently small specimen. However, advances in imaging hold promise that this capability will be available for in vivo measurements.

1. Introduction

The ossicular chain in the middle ear consists of the MIC and the stapes, which transfer vibrations of eardrum into fluid vibrations in the inner ear. This is a very important step in the hearing process. Because these bones are mobile in all three dimensions, the inertial properties are important for a biomechanical model of the middle ear. Inertial properties in the human middle ear bones have been studied [Kirikae 1960; Beer et al. 1996; Weistenhöfer and Hudde 1999], and those values have been widely used for models of the middle ear [Eiber and Freitag 2002; Gan et al. 2002; Koike et al. 2002].

Three-dimensional volume information for the ossicles is necessary to calculate the inertial properties. Such information has been obtained by microscopic surface measurements [Kirikae 1960; Beer et al. 1996; Weistenhöfer and Hudde 1999]. However, this method cannot yield information on the mass distribution inside bone and is not suitable for the complicated features of the middle ear bones. Alternatively, traditional histological methods are used, but they require several months for results. Another issue in modeling the middle ear is the fairly large difference in individual middle ear anatomy. Such a large difference does not allow a nominal middle ear model to be used for all ears. To construct the middle ear

model based on individual anatomy, three-dimensional volume information should be obtained at each stage of manipulation of the specimen, and a nondestructive method is needed. Both microscopic surface measurement and the histological method are destructive.

The microscale X-ray computed tomography (micro-CT) scanner provides nondestructive imaging with resolution as small as 10 μm resolution. The first application of the micro-CT to obtain the general geometry of the middle ear bones [Decraemer et al. 2003; Lane et al. 2004; 2005] found more clarity than with MRI. The present effort extends the method to obtain the quantitative mechanical properties, so some detail of the procedure is given. While the steps involve well-known relations, assembling, generation and interpretation of the images require insight into the mechanics and materials.

2. Material and methods

2.1. *Temporal bone preparation.* Four human temporal bones from three different human cadavers were used (two right ears and one left ear). The ear canal was dissected, the cochlea was removed, and the middle ear cavity was dissected to reduce X-ray attenuation due to materials of no interest for present purposes. The reduction of specimen size also allows increased resolution. Since the focus was on the MIC, the eardrum and stapes were dissected by a surgical laser.

2.2. *Micro-CT scanning.* The vivaCT 40 micro-CT scanner developed by SCANCO Medical AG (see www.scanco.ch) was used in this study. This machine permits control of the resolution, the photon energy, the intensity of the X-ray beam, and the integration time, all of which determine the visibility of the objects of interest.

Scans with higher resolution result in clearer images, especially on micron sized structures such as the ossicles. Figure 1 shows example slice images of the intact ear (left) and the isolated MIC preparation (right) when the resolution of 12.5 μm was obtained with a 25.6 mm diameter holder. This machine allows us to perform high resolution scans up to 2048 × 2048 pixels per image, which correspond to resolutions of 10.5 μm for a 21.5 mm diameter holder. The best resolution of 10.5 μm could be obtained for our specimen by reducing its size to fit into the 21.5 mm diameter holder.

The transmitted photons from an X-ray source to a detector either interact with a particle of matter in their path or pass unaffected [Johns and Cunningham 1974]. The number of photons in the laser beam that are lost due to attenuation in a region of thickness Δx can be represented as

$$\Delta N = -\mu N \Delta x, \tag{1}$$

where N is the total number of impinging photons and μ is a constant of proportionality known as the *linear attenuation coefficient* [Macovski 1983]. The final number of photons N_{out} after traversing an attenuation region of thickness x can be represented by the initial number of photons suppressed by an exponential decay term, the relationship known as Beer Lambert's Law:

$$N_{\text{out}} = N_{\text{in}} e^{-\mu x}. \tag{2}$$

The attenuation coefficient μ depends on the photon energy of the beam and absorption characteristics of the elements as dictated by the quantum mechanical energy levels of the element involved during the absorption process. Since the absorption strength also depends on the mass of the material itself, attenuation coefficients are often characterized instead by the so-called mass attenuation coefficient μ/ρ
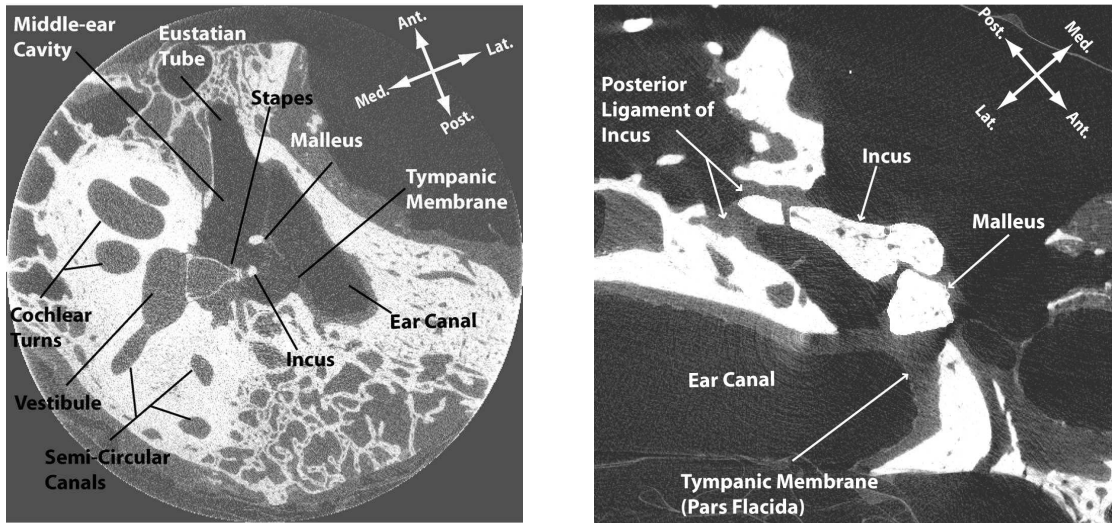
Figure 1. Micro-CT images of intact (left) and isolated MIC (right) from a human temporal bone preparation obtained from $12.5\,\mu$m iso-volume scans with the 25.6 mm diameter holder.

[Johns and Cunningham 1974; Macovski 1983]. Mass attenuation coefficients for body materials show relatively large differences in the lower photon energy regions, where the photoelectric effect is significant. At higher energies, where the attenuation is primarily due to Compton scatter, mass attenuation coefficients become the same for all biological tissues [Macovski 1983]. Even though lower photon energy provides a larger contrast ratio between biological tissues, it is limited by the nonlinear beam hardening artifacts [Brooks and Di Chiro 1976; Wang et al. 1996; Wang and Vannier 1998]. X-ray photons emitted from an X-ray source do not all have the same energy. As an X-ray beam traverses an object, photons within the lower energy spectrum are more readily absorbed and the portion of higher energy photons in the X-ray spectrum increases. Therefore, when high X-ray absorption structures are in the field of view, beam hardening effects are particularly pronounced since photoelectric absorption in bone is high due to the high calcium content.

The vivaCT 40 micro-CT scanner in this study allows 30, 55, or 70 keV as the diagnostic energy level. Because of large interruptions due to beam hardening in bony portions with the lower energy levels, 70 keV was selected as the photon energy, where bones are clearly distinguishable from the background.

The intensity at the detector I_d is given by

$$I_d(x, y) = \int I_o(E) \exp\left[-\int \mu(x, E)\right] dE, \tag{3}$$

where $I_o(E)$ is the incident X-ray beam intensity as a function of the energy per photon E and $\mu(\boldsymbol{x}, E)$ is the linear attenuation coefficient at each region [Macovski 1983; Ketcham and Carlson 2001]. The image clarity depends on the signal-to-noise ratio, which is directly affected by the X-ray intensity. Higher intensities improve the underlying counting statistics, but often require a larger focal spot, which results in degrading image sharpness [Ketcham and Carlson 2001]. The focal spot size of the X-ray tube
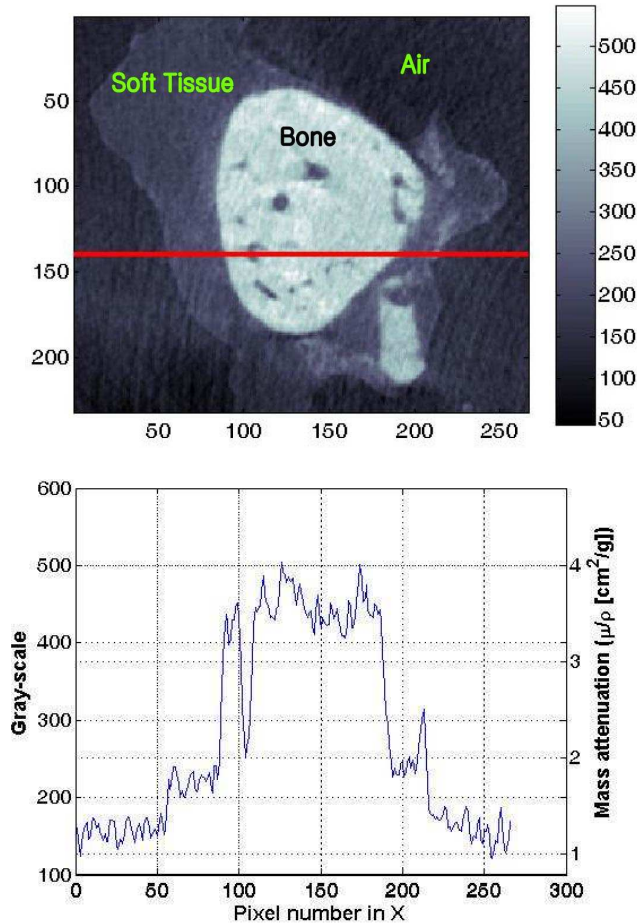
Figure 2. Top: slice image from micro-CT. Bone and soft tissue are distinguishable from surrounding air. Bottom: grayscale along the red line above. Grayscale value of bone has higher range ($350 \sim 550$) than for soft tissue ($200 \sim 350$) and air (below 200).

influences the unsharpness of the final image. Generally the smaller spot size is better for the image sharpness.

The micro-CT scanner used allows the maximum X-ray intensity of $145\,\mu$A, where we could get good signal-to-noise ratio and good image clarity for the default integration time of 380 msec. The typical scan length was about 12 mm for scans in the superior-inferior direction and about 9 mm for scans in the anterior-posterior direction. These values in scan length correspond to approximately 1140 slices and 860 slices at the $10.5\,\mu$m resolution, respectively.

2.3. *Three-dimensional volume reconstruction.* The three-dimensional volume reconstruction from a stack of slices consists of several steps. The first is to outline the object with contours in each slice image. For bone, with high contrast ratio relative to the surrounding soft tissue and air, contours are constructed semiautomatically. Once a contour that approximately matches the shape of the bone is hand-drawn, its shape is adapted to the nearest surface of the bone by a gauss segmentation algorithm. The algorithm is
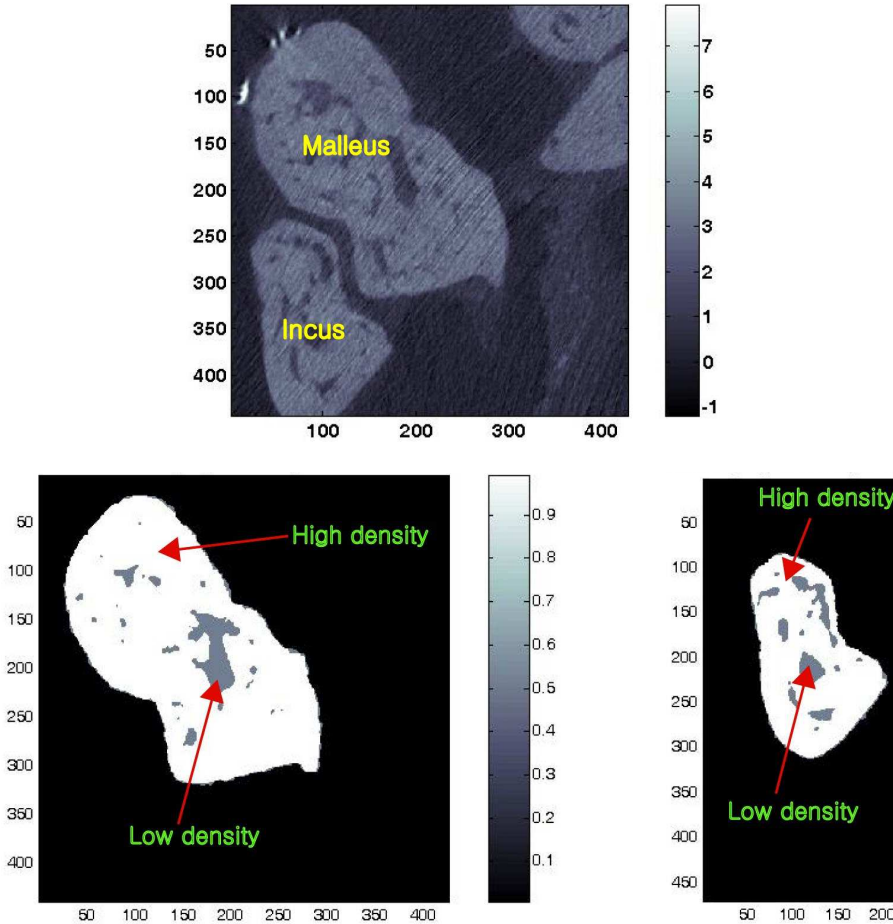
Figure 3. Top: slice image before segmentation. Bottom: segmented slice image of malleus (left) and incus (right). The different threshold values were applied for the low-density part (blood vessels) and high-density part (bone).

repeated until the region of interest (ROI) is judged to be adequately contoured. In essence, the contour *shrink wraps the ROI*. The contour is then copied to the next slice (iterating forward) or the previous slice (iterating backward), and the shrink wrapping procedure is repeated. Once the volume of interest (VOI) is separated from adjacent objects by contours, thresholds in grayscale are applied to identify *full voxel* and *empty voxel*, which correspond to the volume within threshold and out of threshold. Grayscale values in slice images make it easier to select the appropriate thresholds.

Bottom of Figure 2 shows the grayscale values along the red line on top of Figure 2, which were recalculated such that the maximum attenuation ($\mu/\rho = 8 \, \text{cm}^2/\text{g}$) and no attenuation ($\mu/\rho = 0$) correspond to values of 1000 and 0. Grayscale values of 200–350 were set for the soft tissue range. A range above 350 is the range of bone and below 200 is the range for surrounding air.

Figure 3 shows a slice image before (top) and after (bottom) contouring and applying threshold for the malleus (left) and incus (right) bones. After segmenting a stack of slices, they are combined to construct
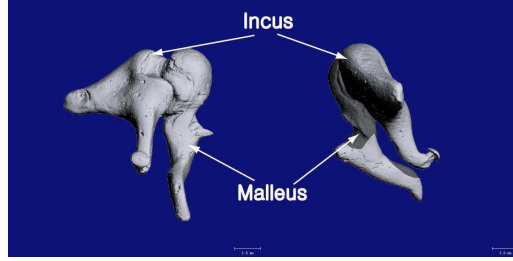
Figure 4. Three-dimensional volume reconstruction of the malleus and incus bones (right ear).

the three-dimensional volume of the object. Figure 4 shows the reconstructed three-dimensional volume of the MIC bones.

2.4. *Calculation of inertial properties.* Portions of the malleus/incus bones are vascularized and thus contain lower-density blood vessels. Consequently, the entire bone cannot be treated as having uniform density; see bottom of Figure 3. The center of mass in the Cartesian coordinate system is calculated with the standard discretization

$$\bar{x} \approx \frac{\sum_{i=1}^{N_L} x_i \Delta m_L + \sum_{i=1}^{N_H} x_i \Delta m_H}{\sum_{i=1}^{N_L} \Delta m_L + \sum_{i=1}^{N_H} \Delta m_H}, \tag{4}$$

while moments of inertia are calculated as

$$I_{xx} \approx \sum_{i=1}^{N_L} (y_i^2 + z_i^2) \Delta m_L + \sum_{i=1}^{N_H} (y_i^2 + z_i^2) \Delta m_H, \qquad I_{xy} \approx -\sum_{i=1}^{N_L} x_i y_i \Delta m_L - \sum_{i=1}^{N_H} x_i y_i \Delta m_H,$$

$$I_{yy} \approx \sum_{i=1}^{N_L} (x_i^2 + z_i^2) \Delta m_L + \sum_{i=1}^{N_H} (x_i^2 + z_i^2) \Delta m_H, \qquad I_{yz} \approx -\sum_{i=1}^{N_L} y_i z_i \Delta m_L - \sum_{i=1}^{N_H} y_i z_i \Delta m_H, \tag{5}$$

$$I_{zz} \approx \sum_{i=1}^{N_L} (x_i^2 + y_i^2) \Delta m_L + \sum_{i=1}^{N_H} (x_i^2 + y_i^2) \Delta m_H, \qquad I_{xz} \approx -\sum_{i=1}^{N_L} x_i z_i \Delta m_L - \sum_{i=1}^{N_H} x_i z_i \Delta m_H.$$

In the above equations, Δm_L is the mass of a *lower-density* voxel and Δm_H is the mass of a *higher-density* voxel. These can be calculated from the physically measured bone mass M and the number of lower-density and high-density voxels N_L, N_H, respectively, with the assumption that the lower-density value ρ_L is just that of water

$$\Delta m_L = \rho_L \Delta v, \qquad \Delta m_H = \rho_H \Delta v = \frac{M - N_L \Delta m_L}{N_H}, \tag{6}$$

where ρ_H indicates the higher-density value and Δv the volume of a single voxel.

Once moments of inertia are known in a given frame, the orientation of a second frame is calculated such that all products of inertia, that is, nondiagonal terms in inertia matrix given by the right side of Equation (5), are zero simultaneously. The principal directions of the second frame and corresponding
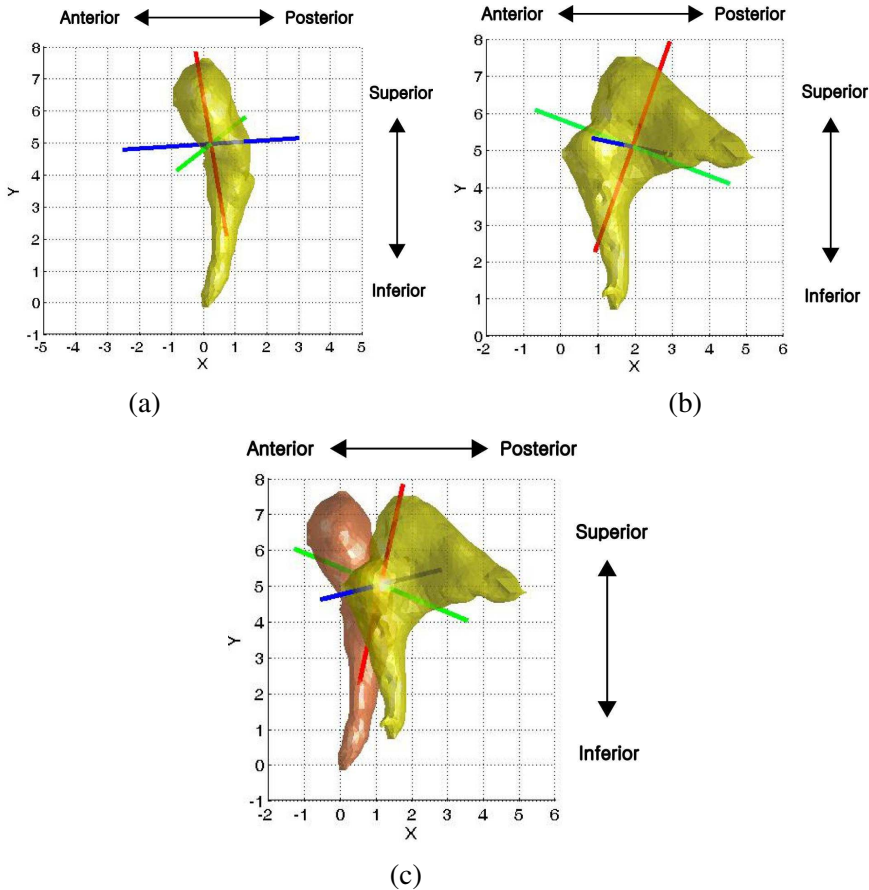
Figure 5. Principal axes of (a) malleus, (b) incus, and (c) MIC of (right) Ear 1. Red line denotes principal axis with minimum principal moment of inertia; blue line denotes maximum.

three principal moments of inertia are calculated from the eigenvalue problem as

$$[I]\{\omega\} = \alpha\{\omega\}, \tag{7}$$

where the three eigenvectors $\{\omega\}$ provide the directions of the principal axes, and the three eigenvalues α the corresponding principal moments of inertia.

3. Results

Figure 5 shows the principal axes of the malleus, incus, and MIC for Ear 1. In this figure, the intersection of the three axes is at the center of mass. The principal axis with the minimum moment of inertia is in nearly the same direction for the malleus, incus and the MIC (red lines in Figure 5), while the direction of the principal axis with the maximum moment of inertia is different (blue lines in Figure 5). The minimum moment of inertia occurs in the superior-inferior direction for the malleus, incus, and MIC.

The malleus has the maximum moment of inertia in the anterior-posterior direction, while incus and the MIC have the maximum moment of inertia in the medial-lateral direction.

Table 1 shows the tabulated mass, density, and the principal inertia measured and calculated from the three-dimensional volume of micro-CT images. Lower-density material within bone, which was measured to consist of 3 to 14% portion of the entire volume, make a relatively small contribution to the dynamic mechanical properties compared to the material of higher density.

Ear 3 has the largest mass and volume, while Ear 2 has the largest density for the malleus and the incus among three specimens. The malleus average density of $2.39 \, \text{mg/mm}^3$ is higher than the incus average density of $2.15 \, \text{mg/mm}^3$ by 11%. The difference between the malleus and incus density is distinguishably large for Ear 2, and only Ear 2 has a heavier malleus than incus.

The principal inertial values of the malleus are consistent with the particular feature of the malleus that length is large compared to the cross section dimensions, by more than a factor of 2. The malleus' moment of inertia along the principal axis of the superior-inferior direction of $17.3 \pm 2.3 \, \text{mg·mm}^2$ is much smaller than the other two principal moments of inertia, which are similar, namely, $106.1 \pm 10.9 \, \text{mg·mm}^2$ and $100.6 \pm 10.1 \, \text{mg·mm}^2$. The values of the principal moments of inertia of MIC are similar for Ears 1 and 2, while for Ear 3, which has much heavier bones than the other ears, these values are much larger, specifically 50% larger for the lateral-medial direction. Ear 1 has smaller principal moments of inertia for the malleus, but larger principal moments of inertia for the incus than Ear 2. Even though three ear samples showed a large diversity in the values of the principal moments of inertia, the ratio of the maximum moment of inertia to the minimum moment of inertia in MIC was about 2 for all three ear samples.

4. Conclusion and discussion

Following previous work of Decraemer et al. [2003] and Lane et al. [2004; 2005], the micro-CT is found to be advantageous for the nondestructive investigation of the middle ear. The procedure for the determination of quantitative geometric and mechanical properties appears to be accurate. Inertial properties of the malleus-incus complex showed significant differences in three ear samples, and also some differences when compared to values found by other procedures by other authors [Kirikae 1960; Beer et al. 1996; Weistenhöfer and Hudde 1999]. For the densities of the malleus and the incus we obtained $2.39 \pm 0.16 \, \text{mg/mm}^3$ and $2.15 \pm 0.07 \, \text{mg/mm}^3$, respectively, while Kirikae [1960] reported 2.27–$4.02 \, \text{mg/mm}^3$ and $1.48 \, \text{mg/mm}^3$ as the corresponding values. Our principal inertial values $132.5 \pm 18.5 \, \text{mg·mm}^2$, $174.5 \pm 21.1 \, \text{mg·mm}^2$, and $259.4 \pm 34.2 \, \text{mg·mm}^2$ of the MIC were slightly larger than the corresponding values $97.6 \, \text{mg·mm}^2$, $165.0 \, \text{mg·mm}^2$, and $217.4 \, \text{mg·mm}^2$ obtained by Weistenhöfer and Hudde [1999]. However, the present results are based on just three ears, so it appears likely that the present and previous values may be correct and indicate the actual variation that occurs in normal ears.

In ongoing work, the dynamic response of the middle ear bones is measured under various conditions with the objective of a better determination of the stiffness properties of ligament attachments. The results from the optimization procedure are sufficiently sensitive that it is important to have the correct inertial properties as input. The simple model for the middle ear consists of a rigid lever rotating about a fixed axis, to represent the ossicular chain, and a rigid piston to represent the eardrum.

Bone	Properties		Ear 1	Ear 2	Ear 3	Mean	SEM
Malleus	Mass		25.9	29.8	35.1	30.3	2.7
	Density		2.14	2.68	2.35	2.39	0.16
	Principal moments of inertia	n_{AP}^M	88.3	103.9	126.0	106.1	10.9
		n_{SI}^M	13.6	16.7	21.5	17.3	2.3
		n_{LM}^M	83.9	98.9	118.9	100.6	10.1
Incus	Mass		29.4	27.8	38.7	32.0	3.4
	Density		2.02	2.23	2.21	2.15	0.07
	Principal moments of inertia	n_{AP}^I	57.4	48.6	72.6	59.5	7.0
		n_{SI}^I	31.8	25.5	48.6	35.3	6.9
		n_{LM}^I	79.1	66.2	107.7	84.3	12.3
MIC	Mass		55.3	57.6	73.8	62.2	5.8
	Density		2.07	2.44	2.27	2.26	0.11
	Principal moments of inertia	n_{AP}^{MI}	149.0	158.2	216.4	174.5	21.1
		n_{SI}^{MI}	114.9	113.2	169.4	132.5	18.5
		n_{LM}^{MI}	223.9	226.4	327.8	259.4	34.2

Table 1. Mass (in mg), density (in mg/mm^3) and principal moments of inertia (in mg·mm^2). SEM stands for standard error of mean. n_{AP}, n_{SI}, n_{LM} denote principal axes in the anterior-posterior, superior-inferior, and lateral-medial directions.

From many measurements and theoretical considerations, it is clear that such a model loses all credibility for frequencies above about 1 kHz. In particular, the ossicular chain has many modes of motion for high frequencies [Eiber and Freitag 2002]. It remains a puzzle how an efficient transfer of acoustic energy takes place with such modes. The present results provide necessary parameters for the analysis of the motion through the audio frequency range and the possibility for an answer to the puzzle.

References

[Beer et al. 1996] H. J. Beer, M. Borniz, J. Drescher, R. Schmidt, H. J. Hardtke, G. Hofmann, U. Vogel, T. Zahnert, and K. B. Hüttenbrink, "Finite element modeling of the human eardrum and application", pp. 40–47 in *Proceeding of the international workshop on MEMRO*, 1996.

[Brooks and Di Chiro 1976] R. A. Brooks and G. Di Chiro, "Beam hardening in x-ray reconstructive tomography", *Phys. Med. Biol.* **21**:3 (1976), 390–398.

[Decraemer et al. 2003] W. F. Decraemer, J. J. J. Dirckx, and W. R. Funnell, "Three-dimensional modelling of the middle-ear ossicular chain using a commercial high-resolution X-ray CT scanner", *J. Assoc. Res. Otolaryngol.* **4**:2 (2003), 250–263.

[Eiber and Freitag 2002] A. Eiber and H.-G. Freitag, "On simulation models in otology", *Multibody Syst. Dyn.* **8**:2 (2002), 197–217.

[Gan et al. 2002] R. Z. Gan, Q. Sun, R. K. J. Dyer, K.-H. Chang, and K. J. Dormer, "Three-dimensional modeling of middle ear biomechanics and its applications", *Otol. Neurotol.* **23**:3 (2002), 271–280.

[Johns and Cunningham 1974] H. E. J. Johns and J. R. Cunningham, *The physics of radiology*, 3rd ed., Thomas, Springfield, IL, 1974.

[Ketcham and Carlson 2001] R. A. Ketcham and W. D. Carlson, "Acquisition, optimization and interpretation of x-ray computed tomographic imagery: applications to the geosciences", *Comput. Geosci.* **27**:4 (2001), 381–400.

[Kirikae 1960] J. Kirikae, *The middle ear*, University of Tokyo Press, Tokyo, 1960.

[Koike et al. 2002] T. Koike, H. Wada, and T. Kobayashi, "Modeling of the human middle ear using the finite-element method", *J. Acoust. Soc. Am.* **111**:3 (2002), 1306–1317.

[Lane et al. 2004] J. I. Lane, R. J. Witte, C. L. W. Driscoll, J. J. Camp, and R. A. Robb, "Imaging microscopy of the middle and inner ear, I: CT microscopy", *Clin. Anat.* **17**:8 (2004), 607–612.

[Lane et al. 2005] J. I. Lane, R. J. Witte, O. W. Henson, C. L. W. Driscoll, J. Camp, and R. A. Robb, "Imaging microscopy of the middle and inner ear, II: MR microscopy", *Clin. Anat.* **18**:6 (2005), 409–415.

[Macovski 1983] A. Macovski, *Medical imaging systems*, Prentice-Hall, Upper Saddle River, NJ, 1983.

[Wang and Vannier 1998] G. Wang and M. W. Vannier, "Computerized tomography", in *Encyclopedia of Electrical and Electronics Engineering*, edited by J. G. Webster, John Wiley & Sons, New York, 1998.

[Wang et al. 1996] G. Wang, D. L. Snyder, J. A. O'Sullivan, and M. W. Vannier, "Iterative deblurring for CT metal artifact reduction", *IEEE T. Med. Imaging* **15**:5 (1996), 657–664.

[Weistenhöfer and Hudde 1999] C. Weistenhöfer and H. Hudde, "Determination of the shape and inertia properties of the human auditory ossicles", *Audiol. Neuro-Otol.* **4**:3-4 (1999), 192–196.

JAE HOON SIM: jhsim@stanford.edu
Mechanics and Computation Division, Department of Mechanical Engineering, Stanford University, 496 Lomita Mall, Durand Building, Stanford, CA 94305-4035, United States

and

Palo Alto Veterans Administration, 3801 Miranda Avenue, Palo Alto, CA 94304, United States

SUNIL PURIA: puria@stanford.edu
Mechanics and Computation Division, Department of Mechanical Engineering, Stanford University, 496 Lomita Mall, Durand Building, Stanford, CA 94305-4035, United States

and

Department of Otolaryngology — Head and Neck Surgery, Stanford University, Stanford, CA 94305, United States

and

Palo Alto Veterans Administration, 3801 Miranda Avenue, Palo Alto, CA 94304, United States

CHARLES R. STEELE: chasst@stanford.edu
Mechanics and Computation Division, Stanford University, 496 Lomita Mall, Durand Building, Stanford, CA 94305-4035, United States